Journal of Photochemistry & Photobiology, A: Chemistry 421 (2021) 113532

Contents lists available at ScienceDirect

Journal of Photochemistry & Photobiology, A: Chemistry

journal homepage: www.elsevier.com/locate/jphotochem

Structural, optical and catalytic properties of $ZnO-SiO_2$ colored powders with the visible light-driven activity

Michael Nazarkovsky [a,*], Bożena Czech [b], Alicja Żmudka [b], Viktor M. Bogatyrov [c], Olena Artiushenko [a], Vladimir Zaitsev [a], Tatiana D. Saint-Pierre [a], Rafael C. Rocha [a], Jiang Kai [a], Yutao Xing [d], Wellington D.G. Gonçalves [e], Amanda G. Veiga [f], Maria Luiza M. Rocco [f], Syed Hamza Safeer [g], Mariia V. Galaburda [c], Victor Carozo [g], Ricardo Q. Aucélio [a], Richard J. Caraballo-Vivas [h], Olena I. Oranska [c], Jairton Dupont [e]

[a] *Chemistry Department, Pontifical Catholic University of Rio de Janeiro, 225 Marquês de São Vicente Str., 22451-900 Rio de Janeiro, RJ, Brazil*
[b] *Department of Radiochemistry and Environmental Chemistry, Institute of Chemical Sciences, Faculty of Chemistry, Maria Curie-Skłodowska University, 3 Maria Curie-Skłodowska Sq., 20-031 Lublin, Poland*
[c] *Chuiko Institute of Surface Chemistry, 17 General Naumov Str., 03164 Kyiv, Ukraine*
[d] *High-resolution Electron Microscopy Lab, Advanced Characterization Center for Petroleum Industry, Fluminense Federal University, Niterói, Rio de Janeiro 24210-346, Brazil*
[e] *Laboratory of Molecular Catalysis, Institute of Chemistry, UFRGS, 9500 Bento Gonçalves Av., 91501-970 Porto Alegre, RS, Brazil*
[f] *Institute of Chemistry, Federal Universityof Rio de Janeiro, 149 Athos da Silveira Ramos Av., 21941-909 Rio de Janeiro, RJ, Brazil*
[g] *Physics Department, Pontifical Catholic University of Rio de Janeiro, 225 Marquês de São Vicente Str., 22451-900 Rio de Janeiro, RJ, Brazil*
[h] *Brazilian Center for Research in Physics (CBPF), 150 Dr. Xavier Sigaud Str., 22290-180 Rio de Janeiro, RJ, Brazil*

A R T I C L E I N F O

Keywords:
$ZnO-SiO_2$ nanocomposite
Photocatalysis
Visible spectrum range
β-Blockers
Carbamazepine

A B S T R A C T

A set of samples of novel colorized zinc oxide-nanosilica composites was synthesized and analyzed. The color and optical properties are directly dependent on ZnO concentration in the composites. Visible light-driven ($\lambda = 550$ nm) catalytic activity on the degradation of pharmaceuticals was tested and indicated that the most active sample with 9 mmol of ZnO per 1 g of SiO_2 was ca. 13 times (toward propanolol), 24 times (toward carbamazepine) and ca. 37 times (toward metoprolol) more effective than blank (catalyst-free photolysis) decontamination. Besides showing a typical charge transfer band on the UV–Vis spectra, all the samples demonstrated a visible light absorbance at ca. 500 nm. Due to the diminution of ZnO particles size, the sample with the minimal concentration of zinc oxide exhibited pronounced luminescence at the region of >500 nm. The microscopy confirmed the decrease of ZnO agglomerated crystalline phase with diminution of ZnO concentration over SiO_2 matrix. XPS studies provided information about the chemical species contributing to the formation of nanocomposites, including the presence of some unexpected trace elements, and also the surface effects of incorporating ZnO nanoparticles into SiO_2 matrix also. With the help of elemental analysis, certain impurities in ZnO were identified, which might be responsible for the outstanding optical and catalytic behavior of the samples. The toxicity results confirmed that applied process can be used for detoxification of wastewater.

1. Introduction

This article continues the study about individual yellowish ZnO with pronounced photocatalytic activity (as under ultraviolet, as visible light irradiation) published in 2017 [1]. As individual ZnO abundant in defects was shown to be active under visible radiation, this research presents another step in understanding the nature of such a behavior combining zinc oxide with fumed SiO_2. Pristine or doped ZnO as a photo-effective material is a well-known case for a large body of research with thorough analysis of its structure in various forms – nanoparticles [2], quantum dots [3], nanorods or nanowires [4], nanowalls [5] and thin films [6]. As a result, the novelty in this area is quite competitive and all published references have to be reviewed critically. Films are less preferred due to the lack of dispersity of the

* Corresponding author.
E-mail address: nazarkovsky_m@esp.puc-rio.br (M. Nazarkovsky).

https://doi.org/10.1016/j.jphotochem.2021.113532
Received 11 February 2021; Received in revised form 12 August 2021; Accepted 30 August 2021
Available online 2 September 2021
1010-6030/

material (less exposed surface at catalytic phenomena) and lower shape factor as compared to isotropic bodies, i.e. spherical particles – 2 and 6, respectively. Thus, quantum effects (near band-gap PL splitting, PL tuning) described in the set forth above studies and associated to the stabilized ZnO by matrix can be controlled during the synthesis. The respective conditions are required to be accurate, repeatable and the "properties-particle size" link has to be predictable within the series of the synthesized samples at any scale (nano or micro). Thus, as a simple, cheap and extensively available matrix, which can facilitate the stated task, fumed nanosilica was selected. Additionally, the implication of alkoxide precursors of SiO_2 is evaded.

Findings on the properties of binary hybrid composites like ZnO-SiO_2 have been consistent as reproducible. By varying the type of SiO_2 matrix (hollow *h*-SiO_2 [7], mesoporous silica [8,9], amorphous silica [10,11], Si-substrate [12]), it becomes possible to establish that SiO_2 affects chemical bond nature for crystalline ZnO and, consequently, indirectly influence spectral characteristics of innovative hybrid materials. SiO_2, as an inert insulator with the band gap of ca. 9.0 eV, enables the homogeneous growth of crystalline ZnO over the surface without blocking pores or pronounced consolidation crystallites. Nanosilica naturally does not participate in the light absorption – the generated charges are concentrated at the interface between the semiconductor catalyst and nanosilica. It acts also as a stabilizer of the reaction intermediates or preventer of the reverse processes and facilitates the charge separation – the smaller the semiconductor size, the less is the probability for the charge self-neutralization [13]. Another advantage of nanosilica is screening off (shielding) the semiconductor nanoparticles while they are formed during the syntheses (hydrolysis or thermal decomposition of the precursors).

The synthesis of binary ZnO/SiO_2 nanocomposites usually intends the formation of zinc oxide through spatial separation within the nanosilica matrix controlling the size of ZnO particles. In addition, the adsorption of zinc compounds accompanied with their oxidative thermal decomposition on silica surface is considered as a process occurring within the space limited by textural pores (gaps among the nanoparticles) and by adsorbed layers which are assigned as nanoreactors. Thus, variable content (ZnO concentration) must control the crystallinity and/or the crystallites size, when at least a weak exciton confinement occurs close to the Bohr radius a_B ($R_{cryst} \geq a_B$, for ZnO is 4.8 nm).

Photocatalytic degradation of pollutants in water or air has gained a great attention recently [14] and the generation of reactive species through the irradiation of photocatalysts surface has been proven to be effective in the treatment of air [15] and water [16].

Beta adrenergic receptor antagonists, β-blockers (BB) are among the widely consumed pharmaceuticals and have been detected in the environmental samples [17]. They are used for regulation of blood pressure, treatment of cardiac, anxiety therapies or angina. Other sources of BB are in veterinary medicine and as illegal doping [18]. Growing consumption of all pharmaceuticals and BB among them will result in increased concentration of these pollutants in the environment [19]. The removal of pharmaceuticals in wastewater treatment plants (WWTP) indicate that some are removed unchanged, some are removed very efficiently while others are difficult to remove and thus, largely remaining in the treated water and return to the environment [20].

In fact, the main route of pharmaceuticals introduction into the environment is treated wastewater, discharge of untreated water or improper management of drugs in municipal waste management system [21]. The fate of the BB and other pharmaceuticals in the environment is connected with their biodegradation, hydrolysis and photodegradation potential and sorption affinity onto sediments or soil. Besides, the transformed products can be more toxic than parent compound [22].

Metoprolol, MTL, e.g. 1-[4-(2-methoxyethyl)phenoxy]-3-(propan-2-ylamino)propan-2-ol) ($C_{15}H_{25}NO_3$, *logP* = 1.88, pK_a = 9.7, M_r = 267.36 g mol^{-1}, Topological Polar Surface Area TPSA = 50.7 $Å^2$) is one of the mostly used β-blockers. Propranolol, PPL, (1-naphthalen-1-yloxy-3-(propan-2-ylamino)propan-2-ol ($C_{16}H_{21}NO_2$, *logP* = 3.48, pK_a = 9.42, M_r = 259.34 g mol^{-1}, TPSA = 41.5 $Å^2$) is one of the mostly detected β-blockers in the environment [23]. The more frequent presence of PPL may be connected with its more hydrophobic character than MTL [22]. It was observed that biotransformation in surface water–sediment systems of PPL required more than 100 days [24] implying also its higher bioaccumulation potential [22].

The other widely found compound in the environment is carbamazepine, CBZ, benzo[b][1]benzazepine-11-carboxamide ($C_{15}H_{12}N_2O$, *logP* = 2.45, pK_a = 13.9, M_r = 236.27 g mol^{-1}, TPSA = 46.3 $Å^2$). CBZ is a tricyclic antidepressants possessing anticonvulsant and analgesic properties [25]. It was reported [26] that CBZ is one of the four most frequently detected pharmaceuticals in soils irrigated with reclaimed water.

37% of PPL and 44% of MT can be eliminated in wastewater treatment plant resulting in up to 1500 ng/L of MTL and 170 ng/L PPL in WWTP effluent [27], whereas the concentration of CBZ was up to 1200 ng/l [28]. Generally, carbamazepine is persistent and low removal rates (usually about 10%) are noted. However, this substance was noted even at the concentration of 3700 ng/L in surface water [29].

In all the cases, the pharmaceuticals possessed TPSA lower than 90, which evidences their ability to penetrate the blood–brain barrier (and thus acting on receptors in the central nervous system). Organics characterized by *logP* in the 0.5–3 range are recognized as simultaneously hydrophilic and lipophilic. These substances can translocate through the lipid bilayer of cell membranes facilitating their transfer to the aerial organs of the plants [30].

The fate of most pharmaceuticals in the wastewater treatment plant is connected with adsorption onto activated sludge or suspended solids where they are bio-transformed and then removed. Application of biological agents during treatment may result in negative removals of some pharmaceuticals [16]. Generally, MTL and PPL revealed poorly removed (up to 20%, removal in WWTP) [31]. The observed "negative" removal, even −362% [32], of CBZ in some WWTPs is connected with the conjugation of 2- and 3-hydroxylated CBZ into parent CBZ during microbiological treatment [16]. After conjugation the increased concentration of CBZ was noticed in treated wastewater [19]. 2-OH-CBZ or 3-OH-CBZ is conjugated to CBZ and then CBZ gets de-conjugated back to 2-OH-CBZ or 3-OH-CBZ making CBZ circulating in the wastewater treatment system. This clearly indicates high recalcitrant character of CBZ. Chlorination is also inefficient in CBZ removal [16].

Despite low environmental concentrations of β-blockers and CBZ, up to a few μg L^{-1}, their wide occurrence makes them possessing hazardous potential on human and animal health [33]. MTL and PPL are considered mobile in the soil structures [22]. The abovementioned low removal rates and environmental fate of BB and CBZ indicate that it is still necessary to develop novel much more effective methods of their removal from environmental matrices [34].

The idea of the present study comprises three aspects: i) determination of structural properties of novel ZnO-SiO_2 composites; ii) determination of their photocatalytic activity; iii) estimation of the new materials potential to eliminate selected β-blockers and pharmaceuticals; iv) verification of the environmental risk of photocatalytically treated wastewater containing MTL, PPL or CBZ.

2. Material and methods

Materials, Materials characterization and the synthesis with the reagents from "RIAP" J.S.C. and fumed silica from "Evonik" are described in the Supplementary File.

2.1. Synthesis of ZnO-SiO_2

Zinc acetate dihydrate (20 g) and carbamide (10 g) were dissolved in distilled water (177.4 mL). Fumed silica was weighted in three separate portions of 4 g each, where 23.28, 46.63, 69.91 g of the zinc acetate/

carbamide solution were added to obtain 3, 6 and 9 mmol of ZnO per 1 g of nanosilica, respectively. The suspensions were subjected to ultrasonic treatment at 22.4 kHz, 1 min. Next, the suspensions were smoothly heated to become xerogels, whereupon the samples were thermally processed at 350 °C (air, 30 min), grinded and calcined again at 600 °C for 75 min to form crystalline ZnO as the main phase. After cooling down, the powders were grinded in an agate mortar and passed through a sieve with a mesh of approximately 0.5 mm.

2.2. Characterization

The obtained materials were characterized by X-ray diffraction (XRD), X-ray photoelectron spectroscopy (XPS), UV–Vis, photoluminescence (PL) spectroscopy, scanning electron microscopy (SEM), inductively coupled plasma mass spectrometry (ICP-MS), CHN analysis and digital image colorimetric analysis.

For the photo-degradation of selected pharmaceuticals a Heraeus photochemical reactor, 0.7 L volume, was used (Fig. S1). In order to understand the impact of ZnO content in the hybrid samples upon the catalytic activity, an extra sample, K-ZnO-SiO_2, containing 18 mmol ZnO per 1 g of SiO_2, was synthesized under identical conditions like other three samples, and applied only in catalytic studies. The activity of photocatalysts was tested under exposure to the visible spectral range (lamp was placed in the center of the reactor emitting light at 500–550 nm with the emittance of 7.5 mW cm^{-2}). The details about the photocatalytic test and all instrumental techniques are presented in Supplementary Information.

3. Results and discussion

All samples exhibited untypical enhanced colorization with growing concentration of Zn^{2+} phase derived from acetate precursor (Fig. 1).

A quantitative description of color is required, since not only the intensity but also some of shades may be altered, which is not obvious for a naked eye. Hence, a digital colorimetric analysis is helpful in the context of the chemical composition in order to avoid speculations and provide numerical characteristics for color. By measuring the effective color intensity of each RGB channel, concentration of ZnO per 1 g of SiO_2 can be estimated using following equations, derived after linear-fitting ($R^2 > 0.990$):

$$C_{ZnO},\ \text{mmol/g} = (A_R - -0.001)/0.01,\ R^2 = 0.9919;$$

$$C_{ZnO},\ \text{mmol/g} = (A_G - -0.004)/0.02,\ R^2 = 0.9976;$$

$$C_{ZnO},\ \text{mmol/g} = (A_B - -0.015)/0.03,\ R^2 = 0.9920.$$

Since the dependence of C_{ZnO} on any separate channel (R, G or B) can be directly computed, at least, within the 3–9 mmol/g range, it concerns for the non-deviation of shades. However, why the combination of two oxides, such as ZnO and SiO_2, characterized as colorless, can result in the visible light absorbing materials must be explained. Therefore, UV–vis diffuse spectra are complement to the digital analysis and visual examinations. As expected, the absorbance at $\lambda \approx$ 450–550 nm increases proportionally to C_{ZnO}. This is not a red shift as had been observed, for example, for ZnO in a previous work [1] – this is a distinct absorbance seen even at the minimal intensity for the sample ZnO-SiO_2-1. No reports have been found describing deep orange ZnO-SiO_2. In the literature stated visible light absorbance around λ = 450–500 nm corresponds to plasmon band-affected ZnO-Ag or ZnO-Au [35,36] as well as for ZnO-SiO_2-Ag [37]; due to doping with cobalt [38], nitrogen [39] or introduction of photosensitizer fluorene-co-thiophene in ZnO [40]. Taking in account a well-distributed phase of ZnO even at 9 mmol/g over nanosilica, the intensity would be associated with pronounced electronic modifications in ZnO. The calculated E_g-s for ZnO-SiO_2-1, ZnO-SiO_2-2 and ZnO-SiO_2-3 are 3.14, 3.02 and 2.97 eV, respectively, and such a slant bears record to possible size change of ZnO crystallites (Fig. 2).

The summary of the facts on optical properties leads us to the simple conclusion that doping is an origin for such a UV–vis profile. In order to exclude all possible atoms that may contribute to the unexpected optical characteristic, ICP-MS and CHN elemental analyses were made. Nitrogen might be important as derived from carbamide O=C(NH_2)$_2$ and might have been incorporated into crystalline lattice of ZnO. The results given in Table 1 support the expectation for atomic doping, whereas the most concentrated metal elements are pointed. The CHN concentrations definitely are not relevant upon the properties, in special, the percentage of nitrogen is too low (<0.3 wt%) to make the discovered effects emerge.

Thus, the colorization of the samples is caused mainly by Mn which, in turn, acts as a dopant whose structure, presumably, invades into decreased ZnO crystallites' lattice provoking imperfections (distortions) resulting in an enhanced luminescence of ZnO-SiO_2-1 shown below. The oxidation state for Mn is assumed as 4+ (octahedral d^3-configuration) - according to the Tanabe-Sugano diagrams, the absorbance is respective to $^4A_2$ – $^4T_2$ transition. This band was detected in the numerous studies on optical materials and emitters [41,42]. Iron or lead cannot exhibit such a profile – Pb^{4+} has no visible-light transition owing to its ionic configuration. In case of Fe^{3+} (d^5-configuration and the ground term ^6S), the only possible band is always attributed to the ligand-to-central ion charge transition: π (O^{2-}) → 3d (Fe^{3+}). The articles dedicated to Fe-doped ZnO-SiO_2 neither report peaks for the 400–500 nm range [43], nor provide UV–vis spectra [44], nor discuss this part clearly [45].

The synthesized series of ZnO-SiO_2 + Mn demonstrates identical colorization and the RGB ratio occurring congruently with the ZnO

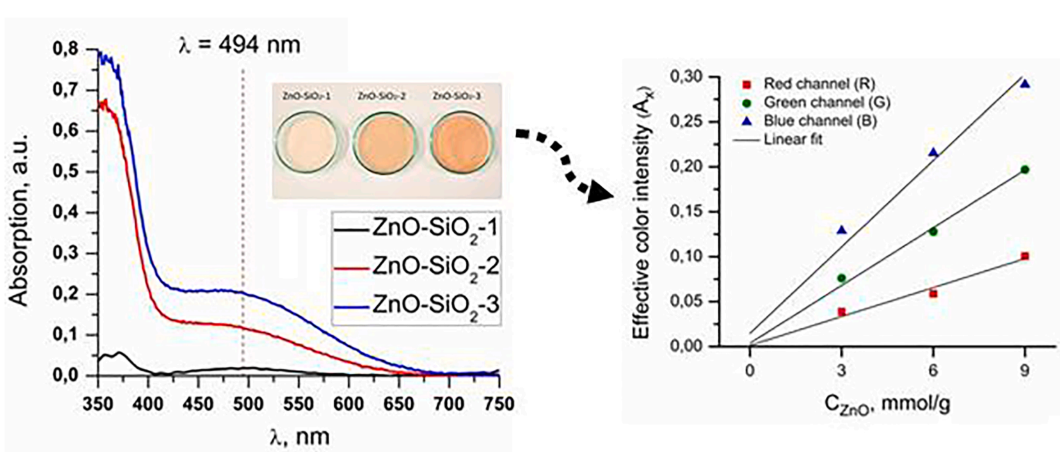

Fig. 1. The UV–vis diffuse spectra of colorized as-synthesized ZnO-SiO_2 samples accompanied with the RGB channel intensity plotted as a function of ZnO concentration in SiO_2.

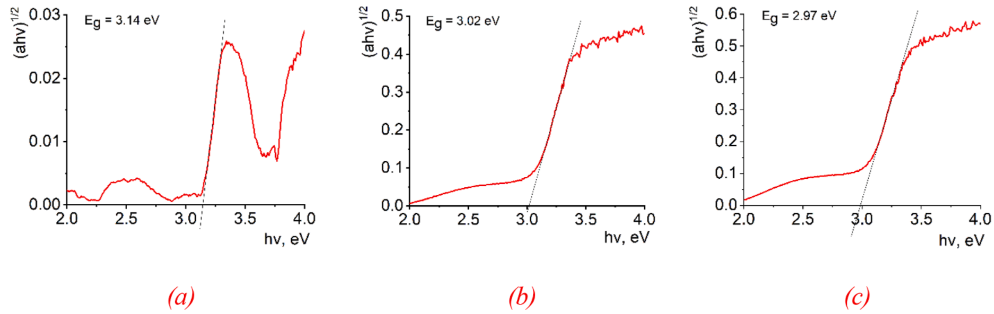

Fig. 2. The Tauc plots for ZnO-SiO_2-1 *(a)*, ZnO-SiO_2-2 *(b)* and ZnO-SiO_2-3 *(c)*.

Table 1
The elemental composition of impurities estimated in the samples from ICP-MS and CHN analyses.

Concentration units	μg/g				wt.%		
Elements	Mn	Fe	Pb	Zn	C	H	N
ZnO-SiO_2-1	34	0	39	272957	0.9	0.5	0.3
ZnO-SiO_2-2	125	135	160	336036	1.6	0.4	0.14
ZnO-SiO_2-3	178	180	216	456497	1.4	0.5	0.13

concentration (Fig. S2), despite reduced linearity for green and red components, as compared to the subject samples. Hence, the presence of the impurities in zinc acetate dihydrate provided by Khimlaborreactiv Ltd. was due to the manufacturer's "fail", whereupon such interesting phenomena are discovered and described below.

Next, the photoluminescence is helpful to crown discussions on optical properties. Illuminated by a lamp (λ = 365 nm) inside a dark chamber (Fig. 3a), the materials are surprisingly discerned by brilliance decreasing with a growing presence of zinc oxide phase and the sample with the minimal ZnO concentration is the most luminescent keeping this property even at excitation at lower energy (Fig. 3b). Also, the main peak for ZnO-SiO_2-1 is slightly shifted to higher energy in comparison to another two samples (at 6 and 9 mmol/g). The latter samples are characterized by less difference in the defect photoluminescence spectral region by their intensities, as compared to an unambiguously visual dissimilarity while excited at higher irradiation in a dark chamber at 365 nm. The visible-light emission in ZnO is well-known and related to the recombination presupposing participation of oxygen vacancies, interstitial structural defects or surface traps. They turn up strongly when the surface-to-volume ratio increases. Thus, it can be emphasized hereby a gradient of the emission which is non-monotonously dependent on the applied energy for two samples - ZnO-SiO_2-2 and ZnO-SiO_2-3.

A distinguishing inhomogeneous luminescence has stimulated a more detailed study by scanning the emission in function of the stepwise variation of the energy of excitation. The cross section of emission showed alterations as in their spectral profile and in intensity (Fig. S3). In lower energy ranges (E_{exc} = 4.5–5.75 eV) the emission was found to be more intense in ZnO-SiO_2-2 with a simultaneous augmentation of two-band-emission with spectral maxima at λ = 420 and 600 nm. At E_{exc} = 5.5 eV, the dissimilarity in the profiles is pronounced: in ZnO-SiO_2-2, two bands are distinguishable and are 1.5 times more intense than the ones observed for ZnO-SiO_2-3.

After accelerating the excitation, the tendency changed to contrary: a lower energy signal (λ = 600 nm) prevailed and more intense for ZnO-SiO_2-3 than for ZnO-SiO_2-2 feature that did not change as excitation energy was increased up to E_{exc} = 7.5 eV. In the same time, the respective peak (600 nm) in ZnO-SiO_2-2 underwent 3 times fading after its maximum at E_{exc} = 5.75 eV. As revealed, a blue signal (λ = 420 nm) decreases and disappears over the whole scan within the 4.5–7.5 eV energy range. This asymmetric behavior found for both materials indicates the important role of different defects contributing to recombination mechanisms as confirmed in an earlier study [46], where the authors came to the same assumption after deconvolution of PL peak at λ = 495–524 nm. These results, in turn, are in a perfect agreement, experimentally proving the conclusion about the connection of increased ZnO/SiO_2 interface with the formation of doubly ionized oxygen vacancies.

Thus, a broad band of ZnO-SiO_2-1 on Fig. 3b can contain a stepped-up blue component whose contribution is a function of the crystallites size of ZnO. In addition, a stable peak at λ = 590 nm remains unchangeable even at blue-shift of the main broad peak in ZnO-SiO_2-1 occurs with enhanced area – this is an extra proof that reducing the crystallites size, the specific defect – $V_o^{\bullet\bullet}$ – becomes more relevant leading to the differentiated optical behavior. The consolidation of the crystallites eveners the blue-component's role in general defect PL, while the only orange-spectrum band is dominating.

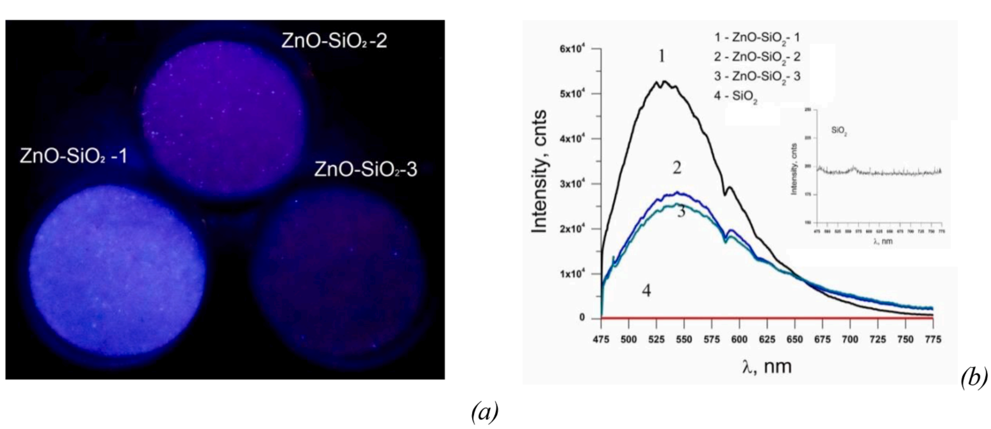

Fig. 3. Luminescence of crystalline phase under λ = 365 nm *(a)* and emission spectra at λ = 473 nm with the PL for SiO_2 (inset) *(b)* irradiation over ZnO-SiO_2-1, ZnO-SiO_2-2 and ZnO-SiO_2-3.

XRD patterns for all samples are shown in Fig. 4, where both the silica amorphous phase contribution, mainly in the diffuse halo over $2\theta = 22.7°$, and Bragg reflections, attributed to crystalline phase, are observed. The Rietveld refinement of the XRD diffractograms was performed with the help of the FullProf software using a standard wurtzite pattern ICDD #79-2205. For ZnO-SiO_2-1, it was impossible to perform an efficient refinement due to low concentration of crystalline ZnO and lack on the respective reflexes, while ZnO-SiO_2-2 and ZnO-SiO_2-3 samples were adjusted pointing out a model where Zn is replaced by Mn at 15 %. In contrast, by using the Scherrer's equation, it was determined the crystallites sizes in samples – 12 nm for ZnO-SiO_2-2 and 13 nm for ZnO-SiO_2-3.

The series of ZnO-SiO_2-1 + Mn, ZnO-SiO_2-2 + Mn and ZnO-SiO_2-3 + Mn is characterized by lower degree of substitution by Mn, i.e. the estimated formula is $Zn_{0.96}Mn_{0.04}O/SiO_2$ and higher values of the crystallites: 20 nm for ZnO-SiO_2-2 + Mn and 21 nm for ZnO-SiO_2-3 + Mn (Fig. S4).

The reduction of the consolidated crystals with the decreasing of ZnO concentration are supported by the SEM images and mappings by EDX (Fig. 5, Fig. S5): ZnO-SiO_2-3 (>1 μm), ZnO-SiO_2-2 (≈ 1 μm), ZnO-SiO_2-1 (<1 μm). Massive crystallites in ZnO-SiO_2-3 intensify colorization of the nanocomposites due to higher bulk density. In contrast, high luminescence in ZnO-SiO_2-1 and the highest absorbance of ZnO-SiO_2-3 are potentially useful in many technical fields of applications with a simple adjusting the structure of the subject oxide hybrids. It is evidence that optical properties, luminescence, morphology and crystal phase size are affected through the present synthesis strategy involving nanosilica as a capping agent. A closer examination of the surface composition via XPS may help in conclusions, as it adds information about the chemical species involved in the formation of the nanocomposites and highlights changes caused by the incorporation of ZnO nanoparticles in the SiO_2 matrix.

The typical survey spectrum and the high-resolution spectra for the Zn2p and O1s core levels of the ZnO-SiO_2-1 sample, which are similar for all analyzed samples, are shown in Fig. 6. From the survey spectrum, the elementary surface composition was obtained. In addition to the expected elements for the ZnO-SiO_2 nanocomposite, traces of carbon, manganese, and lead were observed, which corroborate the results from elemental analysis. Table S1 shows the atomic percentage of the elements present in all synthesized nanocomposites.

The presence of Zn on the surface increases according to the concentration of the nanocomposite, however, this increase is not directly proportional to the increment of zinc oxide in the nanocomposites, which favors the view that with the crystallites growth ZnO might partially diffuse into the bulk.

From the Zn2p spectrum, the Zn2p3/2 peak at 1022 eV is assigned to ZnO-SiO_2 nanocomposite [46]. Yuan reported the higher binding energy of Zn2p in ZnO-SiO_2 in comparison to ZnO pure as being an effect of the formation of Zn-O-Si cross-linking bonds. Due to the difference between the electronegativity of Si (1.9) and Zn (1.65) the charge transfer dynamics are modified decreasing the shielding effect of the valence electrons on the Zn, which cause an increment in the binding energy of the core level [47]. Moreover, no Fe-associated signals were discovered.

The O1s spectrum was deconvoluted into three fitted peaks located at 532.4 eV, 533.4 eV, and 534.5 eV binding energies and assigned to O-Zn, Si-O, and adsorbed water, respectively. An additional feature was observed at 531 eV and attributed to impurities species from ZnO (Table 2). It is notable that with the increase in the concentration of ZnO in the nanocomposite the peak related to the O-Zn bond increases together with the oxygen of impurities while the Si-O bond decreases, which indicates that the crystalline array of the nanocomposite favors the presence of zinc on the surface and the precursor of ZnO is responsible for the presence of possible dopants.

The photo-degradation of pollutants in water was found to be satisfactory (Fig. 7 and Table S2). MTL, PPL and CBZ were poorly degraded by exposure to visible radiation – as only up to 16% (CBZ), 20% (PPL) and 26% (MTL) was decomposed. The removal of MTL was the most efficient in the first 20 min of irradiation (Fig. 7A). Examining the shape of the kinetics curves it can be seen that the process proceeded in two ways. It was similar over the reference photocatalyst (K) and ZnO-SiO_2-2, where photo-degradation was lower and the $\log C_0/C_t$ *versus* time profiles lack linearity. For ZnO-SiO_2-1 and ZnO-SiO_2-3, after a quite fast initial decomposition, further degradation was slower. However, in most cases 60 min of irradiation were enough to remove MTL completely from the solution even for the lowest active photocatalyst (K-ZnO-SiO_2) that promoted 90% degrading of MTL. The obtained data were in agreement with literature, where 87% removal was achieved over self-organized TiO_2 nanotube arrays in 120 min of irradiation [48] or total removal over TiO_2 under performed for 120 min[49] using UV irradiation in both cases. The sorption potential of subject tested photocatalysts, however, differed: 70% of MTL were adsorbed onto ZnO-SiO_2-2 in dark experiment.

Similar behavior was noted for PPL (Fig. 7B). The process was proceeded similarly over two pair of photocatalysts: one pair with ZnO-SiO_2-1 and ZnO-SiO_2-2; and another pair with K-ZnO-SiO_2 and ZnO-SiO_2-3. Interestingly, the shapes of PPL degradation plot observed over ZnO-SiO_2-1 and ZnO-SiO_2-2 are identical and the effect of the concentration of introduced active phase (crystalline ZnO) was too low to enhance the photocatalytic decomposition of PPL. The results obtained over these photocatalysts were about 50% degradation. At higher ZnO

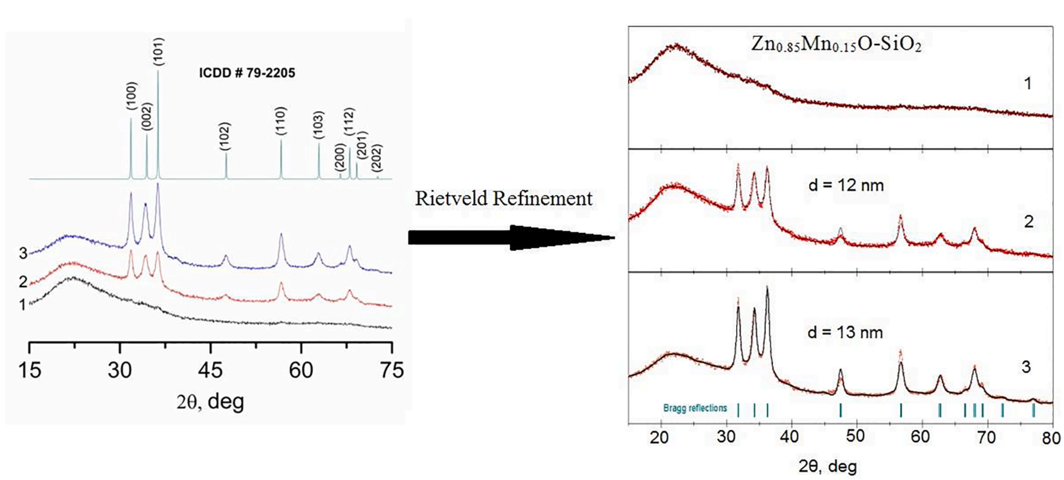

Fig. 4. XRD patterns and Rietveld refinement diffractograms of composites ZnO-SiO_2-1 *(1)*, ZnO-SiO_2-2 *(2)* and ZnO-SiO_2-3 *(3)* supported by the standard wurtzite pattern ICDD #79-2205.

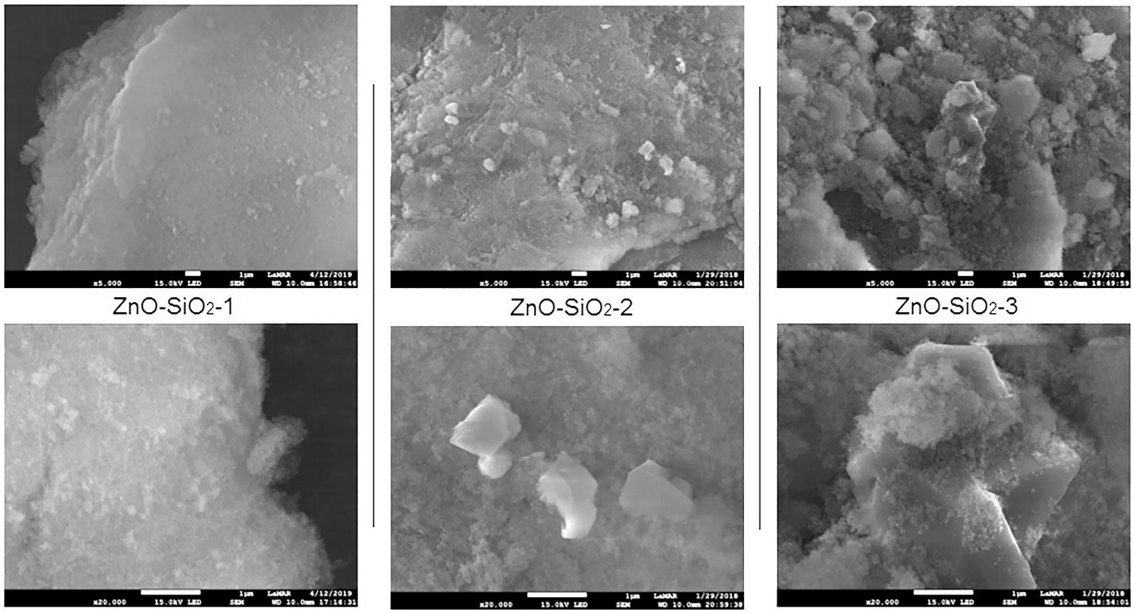

Fig. 5. Secondary electron SEM images of ZnO-SiO_2-1, ZnO-SiO_2-2 and ZnO-SiO_2-3.

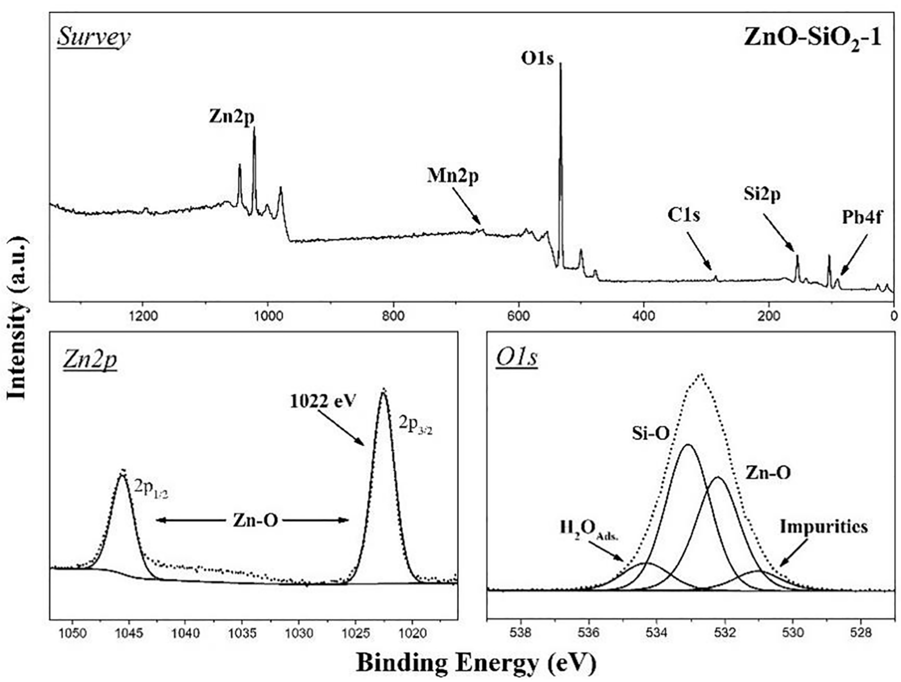

Fig. 6. Survey and core level XPS spectra for the ZnO-SiO_2-1 sample.

Table 2
Deconvolution data from O1s XPS spectrum for all nanocomposites.

Peaks	Atomic %		
	ZnO-SiO_2-1	ZnO-SiO_2-2	ZnO-SiO_2-3
Impurities	6.86	7.36	10.64
O-Zn	37.03	35.52	45.98
O-Si	46.78	37.99	35.46
$H_2O_{Ads.}$	9.33	19.14	7.92

loadings (ZnO-SiO_2-3) the complete removal of PPL was achieved. The PPL removal over Ce(0.5 wt%)-TiO_2 required 90 min under Vis irradiation to be completed [50]. This may point out that the concentration factor of the photocatalyst is stronger than the effects resultant from the quantum-size properties.

The potential of the materials for sorption of PPL was similar – except ZnO-SiO_2-1, where almost no PPL was adsorbed. Others enabled 20% sorption of PPL from 10 mg L^{-1} solution. The dark adsorption of CBZ was also affected by photocatalysts type. The CBZ was adsorbed onto photocatalysts in the following order: ZnO-SiO_2-2 > ZnO-SiO_2-3 > ZnO-SiO_2-1 > K-ZnO-SiO_2. Surprisingly, water treated with K-ZnO-SiO_2 contained slightly higher amount of CBZ than in the case of direct photolysis. It can be explained by the formation of byproducts of CBZ in

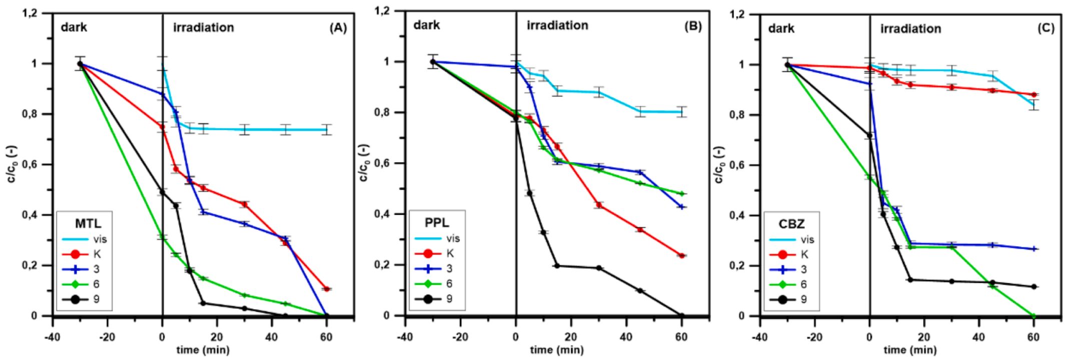

Fig. 7. The kinetics of photocatalytic oxidation of selected pharmaceuticals over tested photocatalysts (A) MTL, (B) PPL, (C) CBZ, [$c_0 = 10$ mg L^{-1}], [$c_c = 0.5$ g L^{-1}], [pH = 6.4]. The set of 3, 6 and 9 corresponds to ZnO concentration (mmol/g) in ZnO-SiO_2.

the course of decomposition which were conjugated and, as a result, promoted an increased response in LC analysis. Most of CBZ decomposition occurred within first 15 min (Fig. 7C). Over ZnO-SiO_2-1 and ZnO-SiO_2-3 the stable by-products were created and no further decomposition of CBZ was observed. Total removal of CBZ was achieved only in case of ZnO-SiO_2-2 irradiated for 60 min. The results were different from described in literature where 96% of the initial concentration of CBZ at 10 mg/L were removed after 30 min of irradiation using P-25 or 93% in the case of ZnO (both under UV irradiation) [51].

The kinetics of pharmaceuticals removal using the photocatalysts can be ascribed to pseudo-first order kinetics only in some extend [52]. The obtained R^2 values are rather low and the lowest values were obtained over ZnO-SiO_2-1: MTL $R^2 = 0.8329$, PPL $R^2 = 0.7228$ and CBZ $R^2 = 0.5719$. The obtained k_1 values ($23.2 \cdot 10^{-3}$–$103.1 \cdot 10^{-3}$ min^{-1}) were higher than noted over TiO_2 nanotubes ($8.6 \cdot 10^{-3}$–$14.4 \cdot 10^{-3}$ min^{-1}) under UV irradiation indicating high potential of the subject photocatalysts in MTL removal.

For PPL, the rate constants, calculated according to the Langmuir–Hinshelwood model, was in the $9.270 \cdot 10^{-3}$–$46.554 \cdot 10^{-3}$ range and lower than that observed by Yang et al. [53] – $182 \cdot 10^{-3}$ min^{-1} during PPL photocatalytic degradation onto TiO_2 under UV irradiation.

Noted, that the range of $k_1 = (1.641$–$53.809) \cdot 10^{-3}$ min^{-1} for CBZ was lower than $113 \cdot 10^{-3}$ min^{-1} observed for CBZ under UV degradation onto ZnO, however, it must be stressed that in cited studies high energetic UV radiation was used [51]. Under UV irradiation, TiO_2 generally was more efficient than ZnO at degrading CBZ [54]. Another example – $k_1 = 17 \cdot 10^{-3}$ min^{-1} – noted for UV degradation over TiO_2 [55].

Interestingly, value of k_1 over the subject photocatalysts statistically correlated with physicochemical properties of the model pollutants. The k_1 obtained over K-ZnO-SiO_2 was strongly ($p < 0.001$) dependent on molar mass of the target pharmaceuticals, indicating that heavier molecules would sorb more efficiently onto nanocomposite. Hydrophilic/hydrophobic properties were crucial in the decomposition rate over ZnO-SiO_2-1 and ZnO-SiO_2-2: the highest *logP* at the lowest k_1 were observed for ZnO-SiO_2-1 ($p < 0.1$) and ZnO-SiO_2-2 ($p < 0.05$). Higher removal rates were proportional to the increasing hydrophilicity of the substrates, which is not associated with pK_a.

In the tested BB molecules, a side chain of ethanolamine was linked by the ether oxygen to the aromatic ring. The presence of oxygen in ether bond increased electron density in the π-system of the aryl group sensitive to the electrophile attack. The deprotonated amine with alkyl substituents [56] is also an electron donor. According to pK_a of all substrates it can be seen that, in neutral conditions, pharmaceuticals –OH group, on the side chain, loses a proton and they were present in protonated forms – $H(PPL)^+$ and $H(MTL)^+$ and only CBZ is in neutral form. Due to the presence of aromatic ring and an aliphatic amino group in MTL at pH < pK_a, the attack of radicals can reach only the aromatic ring. Reactivity was estimated through $pK = pK_a$-log [k(MTL)] + log[k(MTL-H+)] [57]. But it was observed that reactivity of deprotonated amine is 50 times increased in comparison to the aromatic ring [56]. The tests performed at pH 6.4 (original pH of the solutions), indicated the highest MTL removal (Fig. S6A). At lower pH values, the removal was inhibited. In basic conditions the photocatalytic decomposition of MTL was lower than at neutral conditions. Comparison of MTL and PPL indicated that the effect of aromatic ring moiety on photocatalytic degradation rate must be considered. The presence of two ring aromatic moiety in PPL possessing higher electron density may be responsible for its decomposition with the wide pH range [53]. The data clearly indicate that there is no need to correct pH during photocatalytic oxidation of MTL over ZnO-SiO_2 photocatalysts.

The irradiation of the photocatalysts generates highly oxidant radical species, $^{\bullet}OH$ among them. As it can be seen form Fig. S6B, the radical scavengers hindered MTL photocatalytic oxidation over ZnO photocatalysts. The process of MTL decomposition over ZnO proceeds via participation of h^+, $^{\bullet}OH$ and $O_2^{\bullet-}$. However, all the input of all mentioned species was similar. A slight inhibition by Na_2EDTA addition may indicate the highest h^+ impact followed by $^{\bullet}OH$ and $O_2^{\bullet-}$. The participation of photo-generated holes was observed due to the sorption of MTL onto photocatalysts surface. For $^{\bullet}OH$ generation the rate constant for CBZ was estimated at 6.0–$9.9 \cdot 10^9$ M^{-1} s^{-1} (pH 7), MTL 7.3–$8.39 \cdot 10^9$ M^{-1} s^{-1} at 20 °C and pH 7, for PPL $8.7 \cdot 10^9$–$1.1 \cdot 10^{10}$ M^{-1} s^{-1} [58]. Although the oxidation of MTL proceeded both on ZnO surface (for higher amount of MTL adsorbed – via h^+ or surface generated $^{\bullet}OH$) and in solution (via $^{\bullet}OH$). Similarly, $^{\bullet}OH$ and in some extent h^+ were also responsible for MTL and PPL photocatalytic decomposition in the studies of Yang et al.[53].

The produced amino-diol from the cleavage of side chain was observed for all BB during photocatalytic decomposition. The attack of radicals onto PPL molecule considered the attack of the naphthalene ring, and generation of two aldehyde moieties after ring opening [53]. The main products of MTL photocatalytic decomposition were mono-, di-, tri- and tetrahydroxylated intermediates produced due to the addition of –OH. PPL was decomposed into naphthol after the side chain cleavage and some mono-, di- and trihydroxylated intermediates. Nitrogen was removed from BB molecule in the form of NH_3/NH_4^+ as supposed in the literature [53].

Dissolved organic matter is omnipresent in the environment [59]. Due to the physicochemical characteristics and reactivity of DOM [60], it obviously affects the photocatalytic decomposition. In the presence of dissolved organic matter (Fig. S6C) the competition with TA molecules and lowered removal rates were observed. At 10 mg L^{-1} addition of TA the removal efficiency of MTL was lowered from 82% to ca. 60%. Similar effect of organic matter: 4 fold decreased removal was noted in MTL photocatalytic degradation over TiO_2 nanotubes irradiated by vis [48]. The addition of TA was responsible for lowered decomposition as some part of radiation (<380 nm) was absorbed by TA molecules [48]. The sorption of TA molecule onto photocatalysts surface [48] may hinder the sorption of pharmaceuticals affecting photocatalytic process as photocatalytic reaction occurred on or close to the photocatalysts surface [52]. According to Yang et al. [53] adsorption onto photocatalyst surface was of key importance in BB photocatalytic decomposition over TiO_2. The other role of TA was also scavenging of formed reactive species. The photosensitizing role of TA was excluded [48]. The reusability test for ZnO-SiO_2-2 revealed that the loss of activity after 3 runs was not higher than 23% (Fig. S7). Such a loss may be affected by colloidal instability of the composite and/or each recycling can separate individual ZnO particles repeatedly “washed” out from stabilizing silica matrix and floating in the reaction system of the batch reactor.

The TOC diagram (Fig. 8) elucidates the significant difference between the blank test and the catalyzed reaction. The most visible decrease among the substances is for MTL and PPL. CBZ is characterized basically with lower TOC in all tested samples except for ZnO-SiO_2-3, where the level is comparable to the blank. Together with the conclusions taken from the pronounced photodegradation of CBZ, the high TOC for this substance is supposed to be represented mainly by the oxidized intermediates. Obviously, TOC for the blank is attributed to the higher concentration of non-reacted CBZ and less rather to any oxidized products.

The estimating the toxicity of treated wastewater is still needful because the removal of target pollutant is not an indicator of lowered toxicity. Some created by-products with low molecular weight (aldehydes such as formaldehyde or acetaldehyde) or the products of oxidation o natural water constituents have been demonstrated to be toxic to different organisms [16].

As it can be seen from Fig. S9, the highest toxicity to *V. fischeri* was caused by PPL, where total inhibition of the bioluminescence took place. Generally, the toxicity of pharmaceuticals before any treatment was correlated ($p < 0.05$) with its hydrophobicity: the higher *logP*, the higher toxicity. The highest pK_a of pharmaceuticals ($p < 0.05$) corresponds to the lowest toxicity of water after direct irradiation. Interestingly, water containing MTL and treated with ZnO-SiO_2-3 less suppressed the *V. fischeri* bioluminescence (stimulation), confirming that applied process can be used for detoxification of wastewater (Fig. S8).

4. Conclusions

The results have demonstrated that Mn-doping of zinc oxide deposited over nanosilica provokes distinct colorization of the composites with equal contribution of three components (RGB) proportionally to ZnO concentration in the composites (proven by means of XPS, UV–Vis spectroscopy and digital colorimetric analysis with artificially Mn-doped ZnO-SiO_2 series using pure zinc acetate). Photoluminescence properties can be dependent on ZnO crystallites size, proven by XRD, SEM and broadening of the optical band gaps (i), and on the doping having different energy profile while excited at varied energy (ii). All the samples have exhibited the outstanding visible light-induced activity, which is rather attributed to the concentration factor of the photoactive phase than to crystalline size effect. The kinetic constants of pharmaceuticals photodegradation are 3.2–9.1 times (3 mmol/g of ZnO), 2.6–15.2 times (6 mmol/g of ZnO) and 13–37 times (9 mmol/g of ZnO) higher than for blank photolysis. Photocatalytic processes occur involving h^+ (holes), $^{\bullet}OH$ (hydroxyl radical) and $O_2^{\bullet -}$ (oxygen anion-radical) without a preferred portion of any of them. The toxicity tests on *V. fischeri* have shown that among three solutions, the least toxic after-treated pharmaceuticals solution is that one processed with the sample at 9 (maximal) mmol/g of ZnO. Thus, the synthesized materials are of interest as photoluminescent materials and, on the other hand, as visible-light photocatalysts.

Author Contribution Statement

Michael Nazarkovsky. Conception and design of study; manuscript

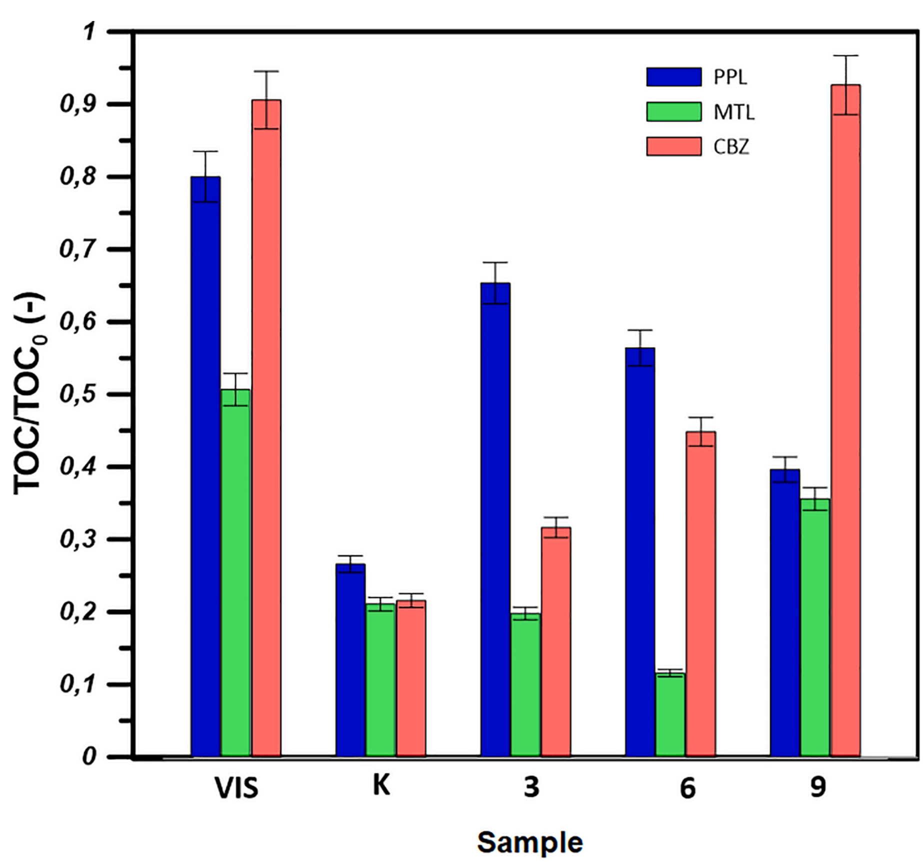

Fig. 8. The TOC progress after 60 min under visible light. The set of 3, 6 and 9 corresponds to ZnO concentration (mmol/g) in ZnO-SiO_2.

preparation and revision; analysis and/or interpretation of data; performance of the characterization procedures: UV-vis, photoluminescence tests.

Bożena Czech, Alicja Żmudka. Manuscript preparation and revision; performance of the photocatalytic, cycling studies and biological tests; acquisition and interpretation of data.

Viktor M. Bogatyrov, **Mariia V. Galaburda.** Synthesis of the composites and participation in the design of the study.

Olena Artiushenko. Performance of the digital image colorimetric analysis and its interpretation.

Vladimir Zaitsev. Providing the project's funds to enable conducting of the present research (CAPES № 2013037-31005012005P5 – PNPD-PUC Rio, Brazil). Advising in the manuscript preparation.

Tatiana D. Saint-Pierre, Rafael C. Rocha. Performance of the ICP tests

Jiang Kai. Providing the project's funds to enable conducting of the 3D scanning of the PL spectra at TGM line of LNLS (CNPEM) – project proposal #20170465. Advising in the manuscript preparation.

Yutao Xing. Performance of the SEM and EDX analysis; manuscript writing; interpretation of data.

Wellington D.G. Gonçalves, Jairton Dupont. The UV-vis measurements; experimental data acquisition; advising in the manuscript preparation.

Amanda G. Veiga, Maria Luiza M. Rocco. Performance of the XPS studies; acquisition and interpretation of data; manuscript writing.

Syed Hamza Safeer, Victor Carozo. Performance of the room temperature PL measurements; acquisition of data; advising in the manuscript preparation.

Ricardo Q. Aucélio. Performance of the CHN studies; advising in the manuscript preparation; manuscript correction.

Richard J. Caraballo-Vivas. The XRD diffraction refinement with the composition prediction from the XRD refinement; interpretation of the data; manuscript writing.

Olena I. Oranska. The XRD analysis performance.

Declaration of Competing Interest

The authors declare that they have no known competing financial interests or personal relationships that could have appeared to influence the work reported in this paper.

Acknowledgements

The authors are grateful to the Coordenação de Aperfeiçoamento de Pessoal de Nível Superior, CAPES (grant № 2013037-31005012005P5 – PNPD-PUC Rio, Brazil) for receiving funds to carry out the research. The authors thank the TGM (Proposal #20170465) beamline from the Brazilian Synchrotron Light Laboratory(LNLS) from the Brazilian Center for Research in Energy and Materials (CNPEM). YTX acknowledges FAPERJ for the support with grant numbers of E-26/010.000978/2019 and E-26/010.001550/2019. Aucélio thanks scholarships from FAPERJ (E-26/202.912/2017) and CNPq (303866/2017-9). This study was also supported by CT-INFRA and FINEP.

About research data

The raw/processed data required to reproduce these findings cannot be shared at this time as the data also forms part of an ongoing study.

Appendix A. Supplementary data

Supplementary data to this article can be found online at https://doi.org/10.1016/j.jphotochem.2021.113532.

References

[1] M.A. Nazarkovsky, V.M. Bogatyrov, B. Czech, M.V. Galaburda, G. Wójcik, O. F. Kolomys, V.V. Strelchuk, M.L. Malysheva, O.I. Oranska, V.M. Gun'ko, Synthesis and properties of zinc oxide photocatalyst by high-temperature processing of resorcinol-formaldehyde/zinc acetate mixture, J. Photochem. Photobiol. A Chem. 334 (2017) 36–46, https://doi.org/10.1016/j.jphotochem.2016.10.040.

[2] O.L. Stroyuk, V.M. Dzhagan, V.V. Shvalagin, S.Y. Kuchmiy, Size-dependent optical properties of colloidal ZnO nanoparticles charged by photoexcitation, J. Phys. Chem. C. 114 (1) (2010) 220–225, https://doi.org/10.1021/jp908879h.

[3] Y.-C. Liang, K.-K. Liu, Y.-J. Lu, Q. Zhao, C.-X. Shan, Silica encapsulated ZnO quantum dot-phosphor nanocomposites: Sol-gel preparation and white light-emitting device application, Chin. Phys. B. 27 (7) (2018) 078102, https://doi.org/10.1088/1674-1056/27/7/078102.

[4] Y. Hao, L. Xu, J. Lei, F. Cui, T. Cui, C. Qu, Self-catalytic synthesis of ZnO nanoparticles@SiO 2 composites with controllable fluorescence, Chem. Lett. 46 (4) (2017) 426–429, https://doi.org/10.1246/cl.161042.

[5] L. Yu, F. Guo, S. Liu, B. Yang, Y. Jiang, L. Qi, X. Fan, Both oxygen vacancies defects and porosity facilitated NO2 gas sensing response in 2D ZnO nanowalls at room temperature, J. Alloys Compd. 682 (2016) 352–356, https://doi.org/10.1016/j.jallcom.2016.05.053.

[6] S. Rajeh, A. Barhoumi, A. Mhamdi, G. Leroy, B. Duponchel, M. Amlouk, S. Guermazi, Structural, morphological, optical and opto-thermal properties of Ni-doped ZnO thin films using spray pyrolysis chemical technique, Bull. Mater. Sci. 39 (1) (2016) 177–186, https://doi.org/10.1007/s12034-015-1132-4.

[7] C. Takai-Yamashita, T. Ishino, H. Razavi-Khosroshahi, M. Fuji, ZnO crystals supported by hollow SiO_2 nanoparticles with fluorescent property, J. Ceram. Soc. Japan. 124 (2016) 239–241, https://doi.org/10.2109/jcersj2.15240.

[8] Z. Shen, H. Zhou, H. Chen, H. Xu, C. Feng, X. Zhou, Synthesis of nano-zinc oxide loaded on mesoporous silica by coordination effect and its photocatalytic degradation property of methyl orange, Nanomater. (Basel, Switzerland). 8 (2018) 317. https://doi.org/10.3390/nano8050317.

[9] R. Malhotra, A. Ali, 5-Na/ZnO doped mesoporous silica as reusable solid catalyst for biodiesel production via transesterification of virgin cottonseed oil, Renew. Energy. 133 (2019) 606–619, https://doi.org/10.1016/j.renene.2018.10.055.

[10] Y. Chen, H. Ding, S. Sun, Preparation and characterization of ZnO nanoparticles supported on amorphous SiO_2, Nanomater. (Basel, Switzerland). 7 (2017) 217. https://doi.org/10.3390/nano7080217.

[11] W. Widiyastuti, S. Machmudah, T. Nurtono, S. Winardi, K. Okuyama, Synthesis of ZnO-SiO2 nanocomposite particles and their characterization by sonochemical method, AIP Conf. Proc. 1840 (2017) 80008, https://doi.org/10.1063/1.4982306.

[12] Y.-Y. Peng, T.-E. Hsieh, C.-H. Hsu, White-light emitting ZnO-SiO2nanocomposite thin films prepared by the target-attached sputtering method, Nanotechnology 17 (1) (2006) 174–180, https://doi.org/10.1088/0957-4484/17/1/028.

[13] D. Zhou, Z. Zhu, B. Liu, Solvothermal synthesis and characterization of a novel reduced graphene oxide (RGO)/BiVO4/SiO2 nanocomposites, Mater. Lett. 185 (2016) 32–35, https://doi.org/10.1016/j.matlet.2016.08.098.

[14] N. Cervantes Rincón, S.B. Hammouda, M. Sillanpää, V. Escobar Barrios, Enhanced photocatalytic performance of zinc oxide nanostructures via photoirradiation hybridisation with graphene oxide for the degradation of triclosan under visible light: Synthesis, characterisation and mechanistic study, J. Environ Chem. Eng. 6 (5) (2018) 6554–6567, https://doi.org/10.1016/j.jece:2018.09.064.

[15] C.-C. Ho, F. Kang, G.-M. Chang, S.-J. You, Y.-F. Wang, Application of recycled lanthanum-doped {TiO}2 immobilized on commercial air filter for visible-light photocatalytic degradation of acetone and {NO}, Appl. Surf. Sci. 465 (2019) 31–40, https://doi.org/10.1016/j.apsusc.2018.09.136.

[16] L.F. Angeles, R.A. Mullen, I.J. Huang, C. Wilson, W. Khunjar, H.I. Sirotkin, A. E. McElroy, D.S. Aga, Assessing pharmaceutical removal and reduction in toxicity provided by advanced wastewater treatment systems, Environ. Sci. Water Res. Technol. 6 (1) (2020) 62–77, https://doi.org/10.1039/C9EW00559E.

[17] V.K. Marothu, M. Gorrepati, N.F. Idris, S.A.M. Idris, R.K.C. Lella, Photocatalysis of β-blockers – An overview, Arab. J. Chem. 12 (7) (2019) 1290–1297, https://doi.org/10.1016/j.arabjc.2014.10.044.

[18] M. Barbieri, T. Licha, K. Nödler, J. Carrera, C. Ayora, X. Sanchez-Vila, Fate of β-blockers in aquifer material under nitrate reducing conditions: Batch experiments, Chemosphere. 89 (11) (2012) 1272–1277, https://doi.org/10.1016/j.chemosphere.2012.05.019.

[19] X. Fan, J. Gao, W. Li, J. Huang, G. Yu, Determination of 27 pharmaceuticals and personal care products ({PPCPs}) in water: The benefit of isotope dilution, Front. Environ. Sci. Eng. 14 (2020) 8, https://doi.org/10.1007/s11783-019-1187-3.

[20] M. Carballa, F. Omil, T. Ternes, J.M. Lema, Fate of pharmaceutical and personal care products ({PPCPs}) during anaerobic digestion of sewage sludge, Water Res. 41 (10) (2007) 2139–2150, https://doi.org/10.1016/j.watres.2007.02.012.

[21] Y. Zhang, P. Chen, S. Liu, P. Peng, M. Min, Y. Cheng, E. Anderson, N. Zhou, L. Fan, C. Liu, G. Chen, Y. Liu, H. Lei, B. Li, R. Ruan, Effects of feedstock characteristics on microwave-assisted pyrolysis – A review, Bioresour. Technol. 230 (2017) 143–151, https://doi.org/10.1016/j.biortech.2017.01.046.

[22] J. Maszkowska, S. Stolte, J. Kumirska, P. Łukaszewicz, K. Mioduszewska, A. Puckowski, M. Caban, M. Wagil, P. Stepnowski, A. Białk-Bielińska, Beta-blockers in the environment: Part {II}. Ecotoxicity study, Sci. Total Environ. 493 (2014) 1122–1126, https://doi.org/10.1016/j.scitotenv.2014.06.039.

[23] J. Maszkowska, M. Wagil, K. Mioduszewska, J. Kumirska, P. Stepnowski, A. Białk-Bielińska, Thermodynamic studies for adsorption of ionizable pharmaceuticals onto soil, Chemos. 111 (2014) 568–574, https://doi.org/10.1016/j.chemosphere.2014.05.005.

[24] M. Ramil, T. El Aref, G. Fink, M. Scheurer, T.A. Ternes, Fate of beta blockers in aquatic-sediment systems: sorption and biotransformation, Environ. Sci. Technol. 44 (3) (2010) 962–970, https://doi.org/10.1021/es9027452.
[25] M.M. Ahmed, S. Chiron, Solar photo-Fenton like using persulphate for carbamazepine removal from domestic wastewater, Water Res. 48 (2014) 229–236, https://doi.org/10.1016/j.watres.2013.09.033.
[26] L. Zhang, S. Du, X. Zhang, G. Lyu, D. Dong, X. Hua, W. Zhang, Z. Guo, Occurrence, distribution, and ecological risk of pharmaceuticals in a seasonally ice-sealed river: From ice formation to melting, J. Hazard. Mater. 389 (2020) 122083, https://doi.org/10.1016/j.jhazmat.2020.122083.
[27] M. Maurer, B.I. Escher, P. Richle, C. Schaffner, A.C. Alder, Elimination of β-blockers in sewage treatment plants, Water Res. 41 (2007) 1614–1622, https://doi.org/10.1016/j.watres.2007.01.004.
[28] R. Fenz, A.P. Blaschke, M. Clara, H. Kroiss, D. Mascher, M. Zessner, Monitoring of carbamazepine concentrations in wastewater and groundwater to quantify sewer leakage, Water Sci. Technol. 52 (2005) 205–213, https://doi.org/10.2166/wst.2005.0135.
[29] Y. Zhang, S.-U. Geißen, C. Gal, Carbamazepine and diclofenac: Removal in wastewater treatment plants and occurrence in water bodies, 73 (n.d.) 1151–1161. https://doi.org/10.1016/j.chemosphere.2008.07.086.
[30] E.M. Beltrán, M.V. Pablos, C. Fernández Torija, M.Á. Porcel, M. González-Doncel, Uptake of atenolol, carbamazepine and triclosan by crops irrigated with reclaimed water in a Mediterranean scenario, Ecotoxicol. Environ. Saf. 191 (2020) 110171, https://doi.org/10.1016/j.ecoenv.2020.110171.
[31] M. Gros, M. Petrović, A. Ginebreda, D. Barceló, Removal of pharmaceuticals during wastewater treatment and environmental risk assessment using hazard indexes, 36 (n.d.) 15–26. https://doi.org/10.1016/j.envint.2009.09.002.
[32] K.O. K'oreje, M. Okoth, H. Van Langenhove, K. Demeestere, Occurrence and treatment of contaminants of emerging concern in the African aquatic environment: Literature review and a look ahead, J. Environ. Manag. 254 (2020) 109752, https://doi.org/10.1016/j.jenvman.2019.109752.
[33] T.A. Ternes, Analytical methods for the determination of pharmaceuticals in aqueous environmental samples, 20 (n.d.) 419–434. https://doi.org/10.1016/S0165-9936(01)00078-4.
[34] J.B. Ellis, Pharmaceutical and personal care products ({PPCPs}) in urban receiving waters, Environ. Pollut. 144 (1) (2006) 184–189, https://doi.org/10.1016/j.envpol.2005.12.018.
[35] S.A. Ansari, M.M. Khan, M.O. Ansari, J. Lee, M.H. Cho, Biogenic synthesis, photocatalytic, and photoelectrochemical performance of Ag–ZnO nanocomposite, J. Phys. Chem. C. 117 (51) (2013) 27023–27030, https://doi.org/10.1021/jp410063p.
[36] Y. Liu, X. Yan, Z. Kang, Y. Li, Y. Shen, Y. Sun, L. Wang, Y. Zhang, Synergistic effect of surface plasmonic particles and surface passivation layer on ZnO nanorods array for improved photoelectrochemical water splitting, Sci. Rep. 6 (2016) 29907, https://doi.org/10.1038/srep29907.
[37] M. Kokate, K. Garadkar, A. Gole, Zinc-oxide-silica-silver nanocomposite: Unique one-pot synthesis and enhanced catalytic and anti-bacterial performance, J. Colloid Interface Sci. 483 (2016) 249–260, https://doi.org/10.1016/j.jcis.2016.08.039.
[38] Y. Lu, Y. Lin, D. Wang, L. Wang, T. Xie, T. Jiang, A high performance cobalt-doped ZnO visible light photocatalyst and its photogenerated charge transfer properties, Nano Res. 4 (11) (2011) 1144–1152, https://doi.org/10.1007/s12274-011-0163-4.
[39] H.-F. Lin, S.-C. Liao, S.-W. Hung, The dc thermal plasma synthesis of ZnO nanoparticles for visible-light photocatalyst, J. Photochem. Photobiol. A Chem. 174 (2005) 82–87, https://doi.org/10.1016/j.jphotochem.2005.02.015.
[40] R. Qiu, D. Zhang, Y. Mo, L. Song, E. Brewer, X. Huang, Y. Xiong, Photocatalytic activity of polymer-modified ZnO under visible light irradiation, J. Hazard. Mater. 156 (2008) 80–85, https://doi.org/10.1016/j.jhazmat.2007.11.114.
[41] Y. Chen, H. Ding, S. Sun, Preparation and characterization of ZnO nanoparticles supported on amorphous SiO2, Nanomaterials 7 (2017) 217, https://doi.org/10.3390/nano7080217.
[42] M. Xia, S. Gu, C. Zhou, L. Liu, Y. Zhong, Y. Zhang, Z. Zhou, Enhanced photoluminescence and energy transfer performance of Y3Al4GaO12:Mn4+, Dy3+ phosphors for plant growth LED lights, RSC Adv. 9 (16) (2019) 9244–9252, https://doi.org/10.1039/C9RA00700H.
[43] R.M. Mohamed, M.A. Al-Rayyani, E.S. Baeissa, I.A. Mkhalid, Nano-sized Fe-metal catalyst on ZnO–SiO2: (photo-assisted deposition and impregnation) Synthesis routes and nanostructure characterization, J. Alloys Compd. 509 (2011) 6824–6828, https://doi.org/10.1016/j.jallcom.2011.03.098.
[44] P. Dhage, A. Samokhvalov, D. Repala, E.C. Duin, B.J. Tatarchuk, Regenerable Fe–Mn–ZnO/SiO2 sorbents for room temperature removal of H2S from fuel reformates: performance, active sites, Operando studies, Phys. Chem. Chem. Phys. 13 (6) (2011) 2179–2187, https://doi.org/10.1039/C0CP01355B.
[45] K. Uma, S. Balu, G.-T. Pan, T. Yang, Assembly of ZnO nanoparticles on SiO2@$α $-Fe2O3 nanocomposites for an efficient photo-Fenton reaction, Inorganics 6 (3) (2018) 90, https://doi.org/10.3390/inorganics6030090.
[46] M.A. Mahjoub, G. Monier, C. Robert-goumet, M. Echabaane, F. Reveret, D. Chaudanson, M. Petit, L. Bideux, B. Gruzza, Synthesis and study of stable and size-controlled ZnO- SiO 2 quantum dots : application as humidity Sensor, (2016). https://doi.org/10.1021/acs.jpcc.6b00135.
[47] Q. Yuan, N. Li, J. Tu, X. Li, R. Wang, T. Zhang, C. Shao, Preparation and humidity sensitive property of mesoporous ZnO-SiO 2 composite, Sensors Actuators, B Chem. 149 (2) (2010) 413–419, https://doi.org/10.1016/j.snb.2010.06.036.
[48] Y. Ye, Y. Feng, H. Bruning, D. Yntema, H.H.M. Rijnaarts, Photocatalytic degradation of metoprolol by {TiO}2 nanotube arrays and {UV}-{LED}: Effects of catalyst properties, operational parameters, commonly present water constituents, and photo-induced reactive species, 220 (n.d.) 171–181. https://doi.org/10.1016/j.apcatb.2017.08.040.
[49] A. Pinedo, M. López, E. Leyva, B. Zermeño, B. Serrano, E. Moctezuma, Photocatalytic decomposition of metoprolol and its intermediate organic reaction products: kinetics and degradation pathway, Int. J. Chem. React. Eng. 14 (2016) 809–820, https://doi.org/10.1515/ijcre-2015-0132.
[50] J. Santiago-Morales, A. Agüera, M. del M. Gómez, A.R. Fernández-Alba, J. Giménez, S. Esplugas, R. Rosal, Transformation products and reaction kinetics in simulated solar light photocatalytic degradation of propranolol using Ce-doped {TiO}2, 129 (n.d.) 13–29. https://doi.org/10.1016/j.apcatb.2012.09.023.
[51] I. Georgaki, E. Vasilaki, N. Katsarakis, A Study on the degradation of carbamazepine and ibuprofen by TiO}2 & {ZnO photocatalysis upon {UV}/visible-light irradiation, Am. J. Anal. Chem. 05 (2014) 518–534, https://doi.org/10.4236/ajac.2014.58060.
[52] D. Friedmann, C. Mendive, D. Bahnemann, TiO2 for water treatment: Parameters affecting the kinetics and mechanisms of photocatalysis, Appl. Catal. B Environ. 99 (3-4) (2010) 398–406, https://doi.org/10.1016/j.apcatb.2010.05.014.
[53] H. Yang, T. An, G. Li, W. Song, W.J. Cooper, H. Luo, X. Guo, Photocatalytic degradation kinetics and mechanism of environmental pharmaceuticals in aqueous suspension of {TiO}2: A case of β-blockers, J. Hazard. Mater. 179 (1-3) (2010) 834–839, https://doi.org/10.1016/j.jhazmat.2010.03.079.
[54] L. Haroune, M. Salaun, A. Ménard, C.Y. Legault, J.P. Bellenger, Photocatalytic degradation of carbamazepine and three derivatives using TiO2 and ZnO: Effect of pH, ionic strength, and natural organic matter, Sci. Total Environ. 475 (2014) 16–22, https://doi.org/10.1016/j.scitotenv.2013.12.104.
[55] A. Jelic, I. Michael, A. Achilleos, E. Hapeshi, D. Lambropoulou, S. Perez, M. Petrovic, D. Fatta-Kassinos, D. Barcelo, Transformation products and reaction pathways of carbamazepine during photocatalytic and sonophotocatalytic treatment, J. Hazard. Mater. 263 (2013) 177–186, https://doi.org/10.1016/j.jhazmat.2013.07.068.
[56] J. Benner, E. Salhi, T. Ternes, U. von Gunten, Ozonation of reverse osmosis concentrate: Kinetics and efficiency of beta blocker oxidation, Water Res. 42 (12) (2008) 3003–3012, https://doi.org/10.1016/j.watres.2008.04.002.
[57] C. von Sonntag, U. von Gunten, Chemistry of Ozone in Water and Wastewater Treatment, {IWA} Publ, IWA Publishing, London, New York, 2012.
[58] S. Mandal, Reaction rate constants of hydroxyl radicals with micropollutants and their significance in advanced oxidation processes, J. Adv. Oxid. Technol. 21 (2018) 178–195, https://doi.org/10.26802/jaots.2017.0075.
[59] Y. Bai, Z. Cui, R. Su, K. Qu, Influence of DOM components, salinity, {pH}, nitrate, and bicarbonate on the indirect photodegradation of acetaminophen in simulated coastal waters, Chemosphere 205 (2018) 108–117, https://doi.org/10.1016/j.chemosphere.2018.04.087.
[60] G.R. Aiken, H. Hsu-Kim, J.N. Ryan, Influence of dissolved organic matter on the environmental fate of metals, nanoparticles, and colloids, Environ. Sci. Technol. 45 (8) (2011) 3196–3201, https://doi.org/10.1021/es103992s.